SMART NANOSENSORS FOR IN-SITU TEMPERATURE MEASUREMENT IN FRACTURED GEOTHERMAL RESERVOIRS

Mohammed Alaskar[1], Morgan Ames[1], Chong Liu[2], Steve Connor[2], Roland Horne[1], Kewen Li[1], Yi Cui[2]

[1]Department of Energy Resources Engineering, Stanford University
367 Panama Street, Stanford, CA 94305-2220, USA
[2]Department of Materials Science and Engineering, Stanford University
496 Lomita Mall, Stanford, CA 94305-4034, USA

e-mail: askar@stanford.edu; mames@stanford.edu; chong813@stanford.edu; horne@stanford.edu;
stconnor@stanford.edu,kewenli@stanford.edu; yicui@stanford.edu

ABSTRACT

Temperature measurements are important for the optimum development and energy extraction of enhanced and conventional geothermal resources. Currently, temperature is only measured in the wellbore, as no technology exists to provide information far into the formation. The development of temperature-sensitive nanotracers could allow for such measurements virtually anywhere in the formation.

This paper describes the synthesis and characterization of two types of temperature-sensitive particles: tin-bismuth alloy nanoparticles and silica nanoparticles with covalently linked dye. Three experiments were performed with the tin-bismuth nanoparticles: a heating test, a slim-tube injection, and a Berea sandstone core injection. Both the heated sample and the effluent samples were characterized using Scanning Electron Microscopy (SEM) and Dynamic Light Scattering (DLS). A heating experiment was also performed with the dye-linked silica particles, and the heated sample was characterized using SEM imaging and fluorimetry.

The feasibility of using nanomaterials as tracers to infer reservoir properties in-situ is addressed.

INTRODUCTION

There is currently no practical way to measure the reservoir temperature and pressure beyond the wellbore region. The overall goal of this research is to develop nanomaterials capable of measuring reservoir temperature and pressure and correlating such information to fracture connectivity and geometry. This idea is based on the fact that certain types of nanomaterials have the property of undergoing observable changes as a function of temperature and pressure, and that nanoparticles are of the appropriate size to fit through the reservoir pore spaces. Temperature-sensitive nanotracers could be used to assess reservoir performance by measuring temperature far from the wells, thereby providing thermal breakthrough information. Temperature-sensitive nanomaterials have already been developed and used in the biomedical industry for drug delivery. Thus, synthesizing temperature-sensitive nanomaterials for geothermal applications is a feasible goal.

Making functional nanomaterials for reservoir sensing involves novel material syntheses to fabricate them and new reservoir engineering approaches to infer reservoir parameters based on the study of their transport properties. Several pressure- and temperature-sensitive nanoparticle concepts have been explored, but are subject to further evaluation from material and reservoir engineering standpoints. Each candidate chosen for investigation will be evaluated according to the following criteria: mobility in reservoir rock, temperature sensitivity, ease of recovery and detection, accuracy of sensing and ease of corresponding analyses, cost, and toxicity.

In order to accomplish the objectives of this study, syntheses of temperature-sensitive nanoparticles were explored for proof of concept and ultimate development. Preliminary heating experiments were conducted to investigate temperature sensitivity, and flow experiments were conducted to investigate the feasibility of transporting these nanoparticles through porous and fractured rocks. The objective was to identify and understand the processes involved in the development and use of tailored nanosensors.

TIN-BISMUTH ALLOY NANOPARTICLES

Tin-bismuth alloy nanoparticles were chosen for our first investigation of temperature-sensitive nanoparticles. This alloy has a melting temperature that is tunable between 139°C and 271°C by

adjusting its composition, as shown in the phase diagram in Figure 1. A simple sensing scheme of melting and subsequent particle growth was conceived. The growth of native gold nanoparticles upon melting in geologic Arsenian pyrite has been observed by Reich et al. (2006) using transmission electron microscopy during in situ heating to 650°C. It was shown that when the gold nanoparticles melted, they became unstable, leading to diffusion-driven Ostwald ripening and ultimately resulting in the coarsening of the size distribution. We hypothesized that upon melting, the size distribution of tin-bismuth alloy nanoparticles would also coarsen.
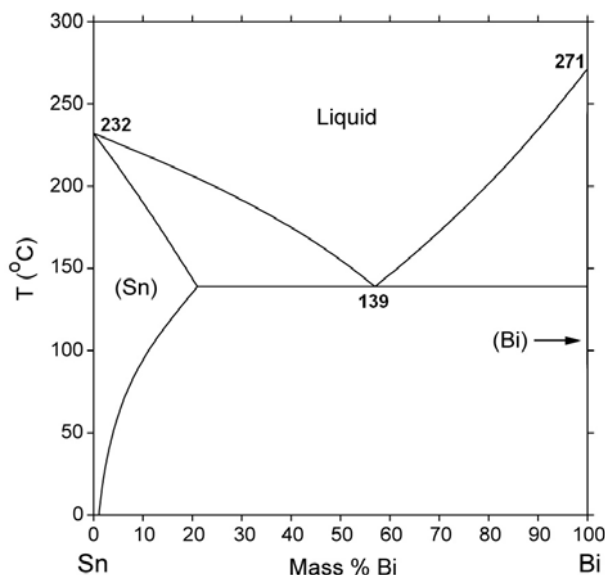

Figure 1: Phase diagram of tin-bismuth (NIST).

Tin-bismuth alloy nanoparticles of eutectic composition were synthesized via ultrasonic processing. These particles were characterized using DLS and SEM imaging. A bench heating experiment was also performed to study the thermal sensitivity of these nanoparticles. The sample was characterized again with DLS and SEM imaging after heating. Injection experiments were performed in a slim-tube packed with glass beads and a Berea sandstone core, and effluent samples were analyzed with DLS and SEM imaging.

Synthesis of tin-bismuth alloy nanoparticles

To perform the synthesis, Sn and Bi were melted together at the eutectic composition (~60 wt % Bi and ~40 wt % Sn). After the alloy was cooled to room temperature, 100 mg was sonicated in 10 ml of mineral oil, a slight variation of the sonochemical method suggested by Chen (2005). The VC-505 ultrasonic processor manufactured by Sonics & Materials, Inc. with a 0.75 in. diameter high gain solid probe was used. The sonicator was operated at 200 W (~95% amplitude) with a pulse setting of 20 s

on, 10 s off. The mixture was cooled to room temperature. The alloy particles were washed and centrifuged several times with a 1:1 mixture of hexane and acetone, rinsed in a solution of 0.1 M polyvinyl pyrrolidone (PVP) in ethanol, and finally suspended in ethanol. The centrifuge setting was 6000 rpm for 15 minutes each time.

Characterization of tin-bismuth alloy nanoparticles

The tin-bismuth alloy nanoparticles were characterized in terms of size and shape using DLS and SEM imaging.

It was determined from three consecutive DLS measurements that there was a wide distribution of the particle hydrodynamic diameter, as shown in Figure 2.
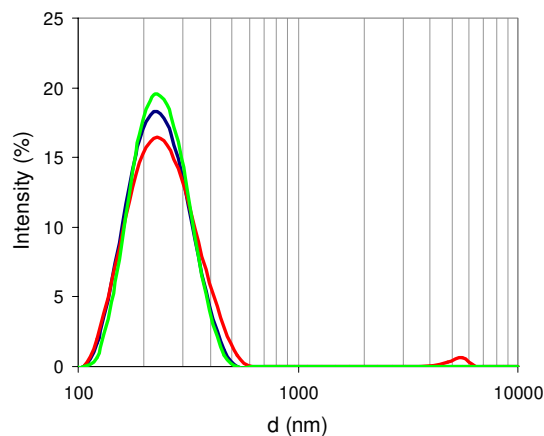

Figure 2: Logarithmic particle size distribution based on hydrodynamic diameter for original tin-bismuth nanoparticle sample.

The three measurements are in reasonable agreement, with an average modal value of 235 nm. The hydrodynamic diameter ranged from ~100 nm to ~600 nm, with Run 2 showing a small peak at ~5500 nm. This indicates that there may have been large particles in the sample, either due to aggregation or from the original synthesis.

The SEM images of the sample show good agreement with the DLS measurements, as shown in Figures 3 – 5.

It is apparent from Figures 3 – 5 that the tin-bismuth nanoparticles range from 50 nm to less than 600 nm. Furthermore, although many of the nanoparticles seem to be spherical as expected, the presence of nonspherical crystalline structures indicates that the sonochemical synthesis did not reach completion. Aggregation on the substrate is observed in both

figures, but it is unclear whether this aggregation occurs in solution or upon drying on the substrate. The DLS results suggest that the latter may be the case.
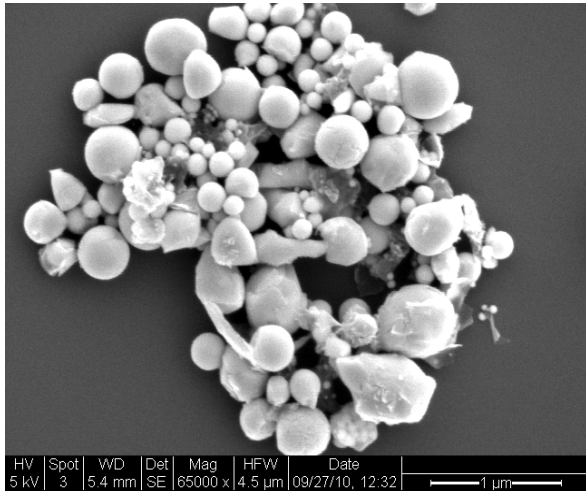

Figure 3: SEM image showing the wide range of tin-bismuth nanoparticle sizes.
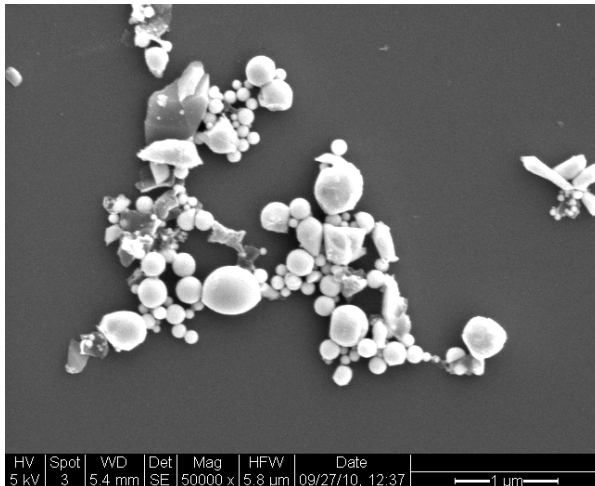

Figure 4: SEM image showing the wide range of tin-bismuth nanoparticle sizes.
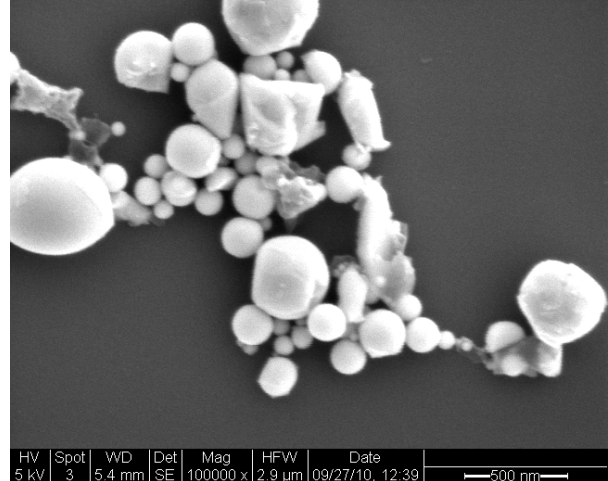

Figure 5: SEM image of tin-bismuth nanoparticles at higher magnification.

Tin-bismuth nanoparticle heating experiment

To begin investigating the melting behavior of tin-bismuth nanoparticles within the temperature range of interest, a sample of the nanofluid (tin-bismuth in mineral oil) was subjected to a preliminary heating experiment. Although ultimately we are interested in the melting behavior of the tin-bismuth nanoparticles in water, the heating experiments were performed in oil due to the complications associated with the boiling of water at experimental conditions. As shown in the phase diagram Figure 1, at the eutectic composition, the tin-bismuth alloy melts at 139°C. In fact, the nanoparticles likely melt at a slightly lower temperature than this due to melting point depression due to their size.

Experimental methods used in heating

The sample was heated using a heating mantle connected to a temperature controller with a feedback thermometer, as shown in Figure 6.
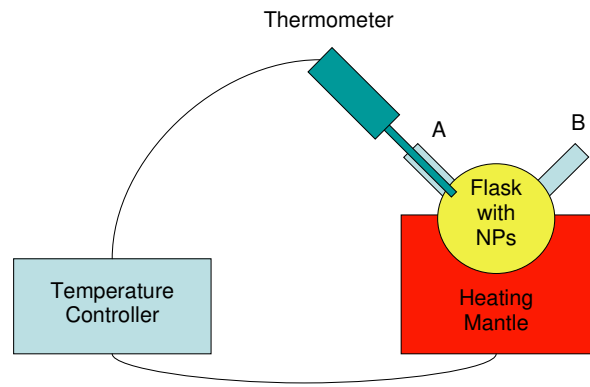

Figure 6: Experimental apparatus for tin-bismuth heating experiment

The flask containing the tin-bismuth nanoparticles in oil was placed in the heating mantle, which was connected to the temperature controller. The temperature controller was also connected to a thermometer, the feedback from which affected whether the mantle was heated, cooled, or maintained and the rate at which this was done. The thermometer was positioned in port A.

The sample was heated in steps to the expected melting point of 139°C. The sample was monitored for a color change near the expected melting point, and when none occurred, the sample was heated in steps to 210°C. No color change ever occurred, but the heating was stopped to prevent the mineral oil from burning. Also, it is likely that melting occurred regardless of the absence of color change. Finally, when the apparatus was at room temperature, the sample was removed from the flask.

The sample was then washed and centrifuged several times with a 1:1 mixture of hexane and acetone, rinsed in a solution of 0.1 M PVP in ethanol, and finally suspended in ethanol. The centrifuge setting was 6000 rpm for 15 minutes each time. This sample was characterized using DLS and SEM imaging.

Heating experiment results

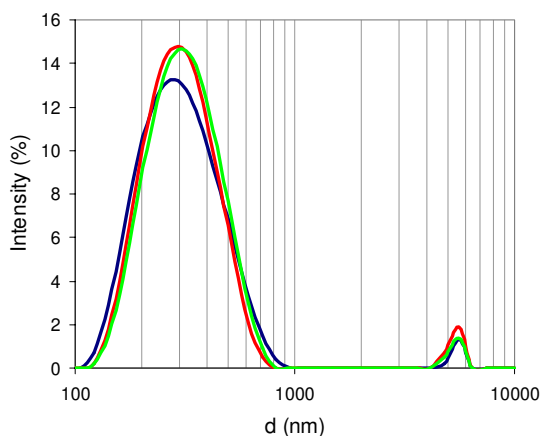The DLS results of the sample subjected to heating are shown in Figure 7.

Figure 7: Logarithmic particle size distribution based on hydrodynamic diameter for heated tin-bismuth nanoparticle sample.

The three measurements are in relatively close agreement, with an average modal value of 321 nm. The hydrodynamic diameter ranged from ~100 nm to ~1000 nm. Appreciable secondary peaks in the range of ~4100 nm to ~6400 nm were observed for all runs. This indicates that there are large particles in the sample, most likely due to aggregation and fusion of the particles. Selected particle size distribution curves

for comparison of the original and heated samples are shown in Figure 8.

As shown in the figure, the particle size distribution peak shifted noticeably to a larger size. Also, the secondary peak in the micron scale is noticeably larger, indicating that there are more large aggregates. SEM images of the heated sample are shown in Figures 9 and 10.
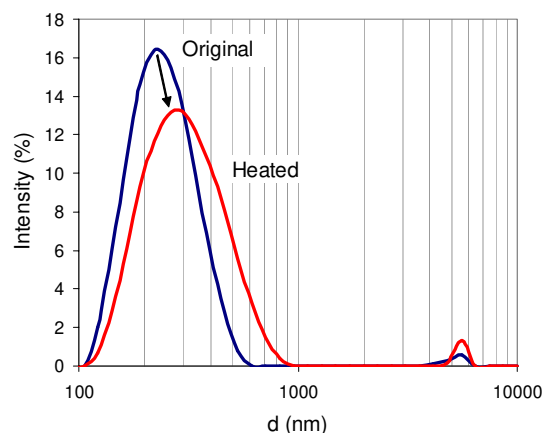

Figure 8: Comparison of logarithmic particle size distribution based on hydrodynamic diameter for original and heated tin-bismuth nanoparticle samples.
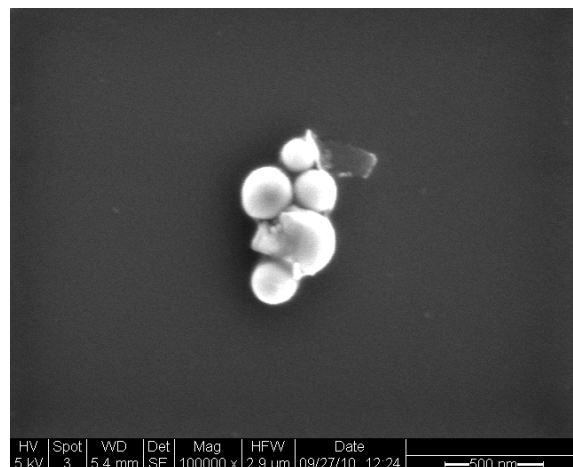

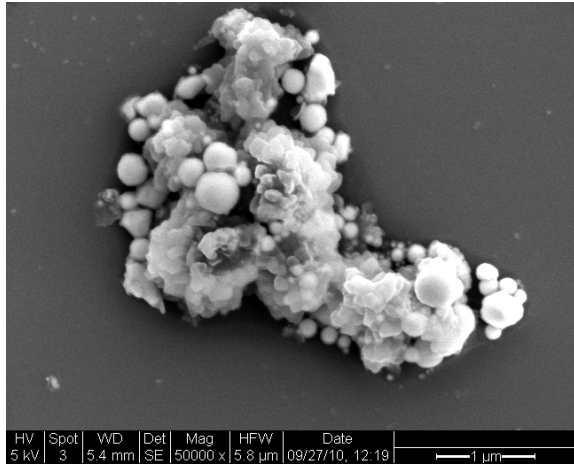*Figure 9: SEM image showing heated tin-bismuth nanoparticles.*

Figure 10: SEM image showing large aggregate of heated tin-bismuth nanoparticles.

Figure 11: Polypropylene slim tube packed with glass beads.

Fusion of melted particles can be observed in both figures, and the sizes of both particles and large aggregates are within the range suggested by DLS results. While the fusion of melted particles could account for the shift in particle size distribution, it is difficult to reach any definite conclusions from the SEM results due to the very wide particle size distributions of both the heated and unheated samples. To avoid this ambiguity, the synthesis will be repeated with adjusted parameters in order to achieve a more uniform particle size distribution. Additionally, heating experiments will be repeated directly on a silicon substrate, and a small region of this substrate will be marked for unambiguous SEM analysis.

Tin-bismuth nanofluid injection experiments
Because of the temperature sensitivity of the tin-bismuth alloy nanoparticles and their potential to be used as a geothermal resource temperature sensor, transport of these particles through porous media was investigated. The nanoparticle suspensions were injected into a slim tube packed with glass beads and into a Berea sandstone core.

Berea sandstone and slim tube characterization
The porosity of the core sample was measured by resaturation with pure water and found to be around 17.5% with pore volume in the order of 10 cm^3.

The liquid permeability was measured by introducing pure water at different flow rates ranging from 1 to 5 cm^3/min. The average permeability was found to be approximately 125.4 md. By mercury intrusion, it was found that the sandstone core has pore sizes in the range from 0.01 to 20 μm.
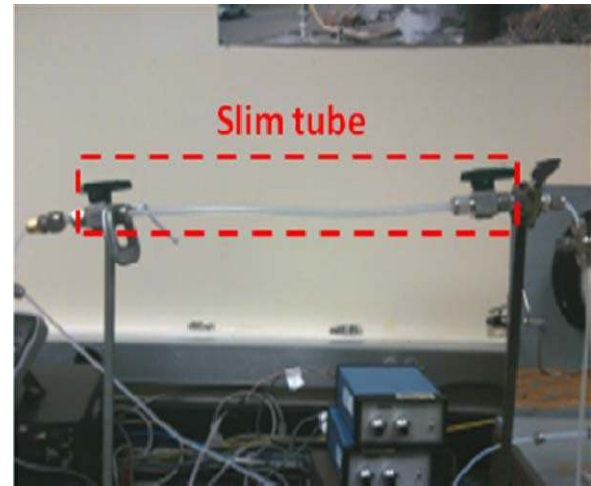
To investigate the mobility of nanoparticles in the absence of rock materials (such as clays), the nanoparticles were injected into a slim tube packed with glass beads. A 30 cm long polypropylene slim tube was constructed. The tube was packed with glass beads (Glasperlen 0.1 cm in diameter from B. Braun Biotech International) and fitted with screens and valves at each end. This polypropylene slim tube is pictured in Figure 11. The permeability and pore volume of the slim tube packed with glass beads were found to be approximately 18.1 md and 2.6 cm^3, respectively.

Experimental methods used in injection
Tin-bismuth nanoparticle injections were conducted to investigate their flow mechanism through the pores of Berea sandstone. The apparatus used is depicted in Figure 12. Nanofluid solution was contained in a pressure vessel downstream of the water pump. The nanoparticles were injected with the aid of nitrogen gas.

Initially, the core was preflushed with several pore volumes of pure water to displace rock fines and debris. About 30% (3 cm^3 of nanofluid) of the pore volume was then injected. Subsequent to the injection of the nanofluid, a post injection of 13 pore volumes of pure water was introduced. In addition, the core was backflushed with 5 pore volumes in attempt to mobilize nanoparticles that might be trapped at the inlet of the core. The injection was at the rate of 1 cm^3/min. A total of 40 effluent samples were collected at the rate of 2 cm^3 per sample. The effluent sample volume was increased to 6 cm^3 for the last six pore volumes. During the backflushing of the core, the flow rate was varied between 1 to 5 cm^3/min. The higher flow rates were used to investigate their effect on the mobility of the nanoparticles. SEM imaging was used to analyze the selected effluent samples.

Injection experiment results

Tin-bismuth nanoparticles were identified in a few effluent samples in very low concentrations. It was observed that only nanoparticles with diameters 200 *nm* and smaller were transported within the pore spaces of the rock, as shown in the SEM image in Figure 13A. Note that the influent sample (Figure 3) contained nanoparticles as large as 600 *nm*. It was speculated that larger particles (greater than 200 *nm*) were trapped at the inlet of the core. In fact, SEM imaging of the backflushing effluents showed that there was entrapment of various nanoparticle sizes, including the sizes greater than 200 *nm* (Figure 13B). The rock filtered the nanofluid injected allowing only a certain particle sizes to flow across it. It should be noted that this is a qualitative analysis in which the determination of the relative numbers of particles recovered was not possible.
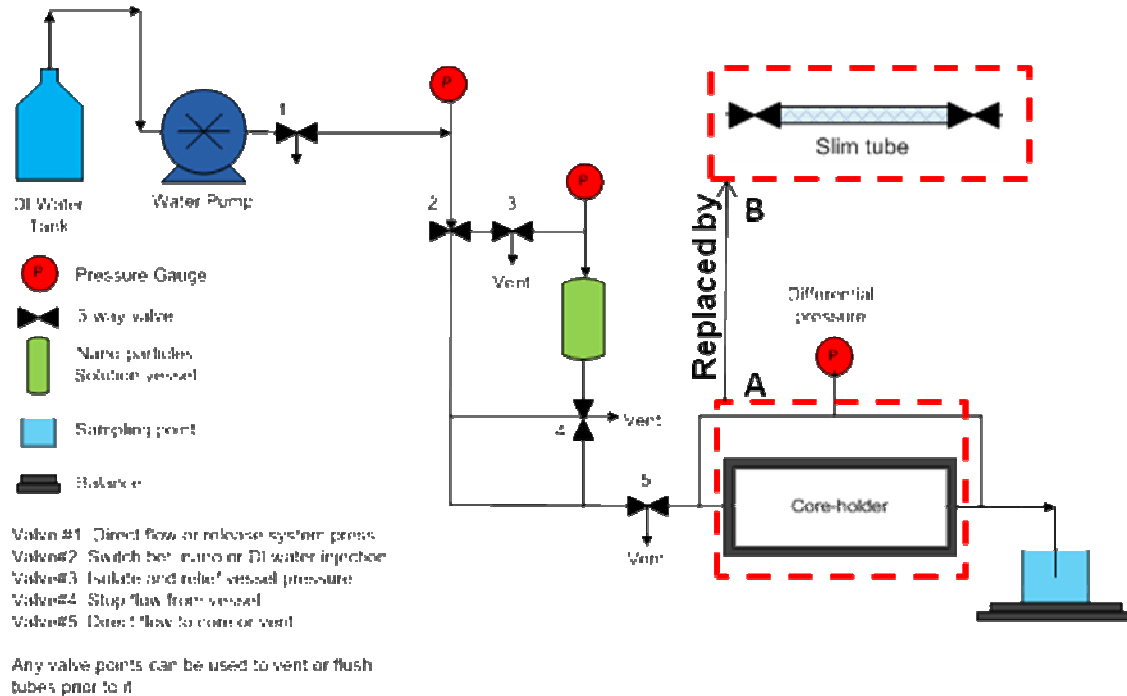

Figure 12: Schematic of the flow experiment apparatus used for injections into (A) core plug and (B) slim tube packed with glass beads.
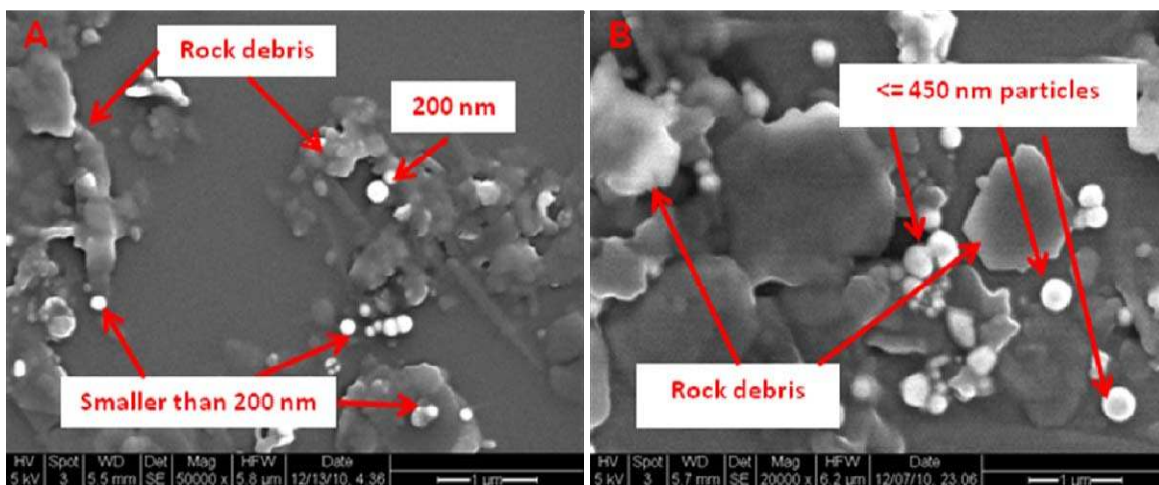

Figure 13: SEM imaging showing the tin-bismuth nanoparticles at the effluent during (A) injection and (B) backflushing of the Berea sandstone. Only particles smaller than 200 nm transported through pore spaces while larger particles trapped at the inlet of the core and mobilized during backflushing.

The permeability measurements during the injection agree with this finding. The permeability as a function of the injected volume is depicted in Figure 14. There was a sudden drop in permeability to about 56% of the original value, after which the permeability remained at that level during the first post injected pore volume, indicating the partial plugging of the pores. Then, permeability started to increase until reached a plateau at approximately 82% of its value prior to the nanofluid injection. At this time, only nanoparticles of 200 *nm* and smaller were observed in the effluent, using SEM (Figure 13A). As mentioned earlier, the backflushing of the core mobilized some particles and as a result the permeability of the rock improved slightly by 8% (i.e. back to 90% of its original value).

However, permeability improvement (from 56% to 90% of original value) does not imply a good recovery of the injected nanoparticles. If the injected nanofluid has a visible color, it is possible to observe the nanoparticles in the effluent visually. In the case of the tin-bismuth injection, the influent had a dark gray color that was characterized by being highly concentrated with nanoparticles. All effluent samples appeared transparent, so it was hypothesized that many of these nanoparticles were trapped within the rock pores, most likely at the inlet of the core. Examining the pore spaces of the rock itself confirmed that considerable numbers of the tin-bismuth nanoparticles were trapped (Figures 15 and 16).
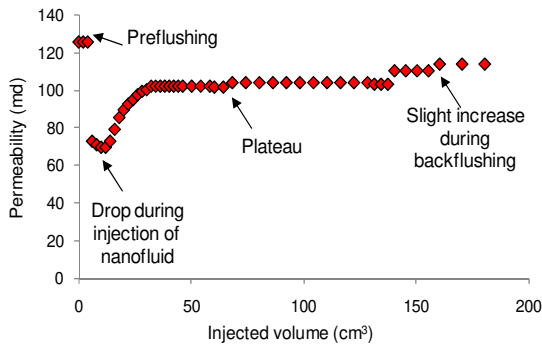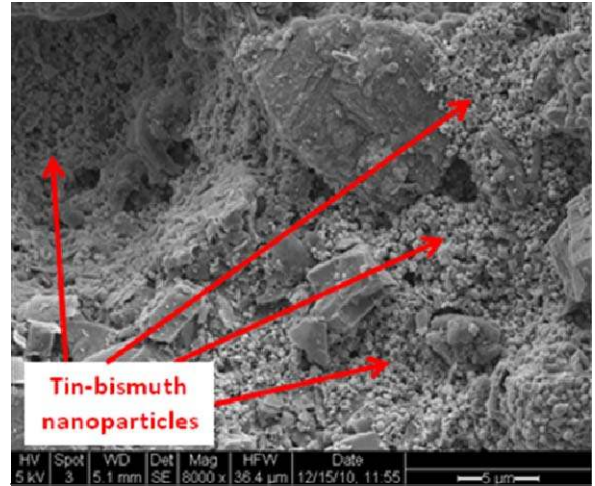

Figure 15: SEM image of the pore space at the inlet of Berea sandstone used during the tin-bismuth injection. Nanoparticle entrapment is apparent.

Further evaluation using SEM imaging (Figure 16) of the rock pore spaces demonstrates the bridging and plugging of the tin-bismuth nanoparticles in the pore throat entry. Kanj et al. (2009) explained that small particles of high concentrations might bridge across the pore throat. The authors also added that larger particles could result in direct plugging of the pore entry. Both phenomena would impact the rock permeability negatively. Particles shown in Figure 16 could not be mobilized either by increasing the injection flow rate or by backflushing and were probably responsible for the permanent reduction in the rock permeability.
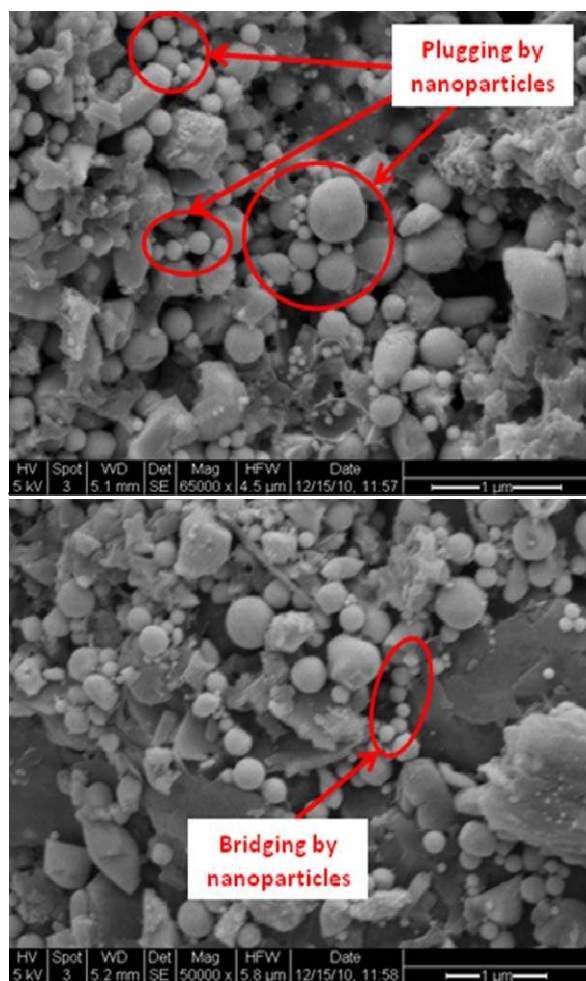

Figure 14: Permeability measurements during the injection of the tin-bismuth nanoparticles.

Figure 16: SEM images from within the pore spaces of the Berea sandstone. They demonstrate the bridging and plugging phenomena.

The SEM analysis did not provide conclusive evidence of the mechanism of particle entrapment. Alaskar et al. (2010) reported that the nanoparticles' shape and surface characteristics play a major role in their transport through a porous medium. They also reported that the spherical silicon dioxide (SiO_2) nanoparticles with narrow size distribution and surface charge compatible to that of the rock were transported successfully through the pore spaces of Berea sandstone. SiO_2 nanoparticles were not trapped in the pore spaces by hydraulic, chemical or electrostatic effects. The tin-bismuth nanoparticles exhibit similar properties in terms of shape and surface charge (negatively charged), except that the tin-bismuth nanoparticles had a wide distribution of sizes between 50 to 600 *nm* (Figure 2 and 3). Thus, particle shape and surface charge should not impose flow constraints. The optimized testing program suggested by Kanj et al. (2009) emphasizes particle size, influent concentration and affinity of particles to rock matrix.

In the case of tin-bismuth injection, although the influent sample had wide distribution of particle sizes, they were all within the size of the pore network. Therefore, it was concluded that the tin-bismuth nanoparticles affinity and/or concentration may have caused their entrapment.

Further investigation of particle affinity to Berea sandstone was carried out by injecting the same influent sample with identical concentration to a slim tube packed with glass beads. This allowed testing the transport of the tin-bismuth nanoparticles in the absence of the core material. One pore volume of the nanofluid was injected at the rate of 0.5 *cm³/min* followed by continuous injection of pure water at the same rate. Several effluent samples were collected and analyzed by SEM imaging.

It was found that the tin-bismuth nanoparticles of all sizes flowed through the slim tube. The increasing concentration of the nanoparticles was observed visually through the injection of the first post-injected pore volume as illustrated in Figure 17. SEM imaging confirmed this finding as depicted in Figure 18.

Thus, it has been demonstrated that the spherically shaped tin-bismuth nanoparticles can be recovered following their injection into tube packed with glass beads without being trapped within the flow conduits, but not through the pore network of the rock (which has much smaller pores). This might be attributed to an affinity of these nanoparticles to the sandstone rock matrix or high nanoparticle concentration imposing constraints to their flow. The complexity of the rock pore network compared the large pores in the glass beads was not taken into consideration during this analysis.
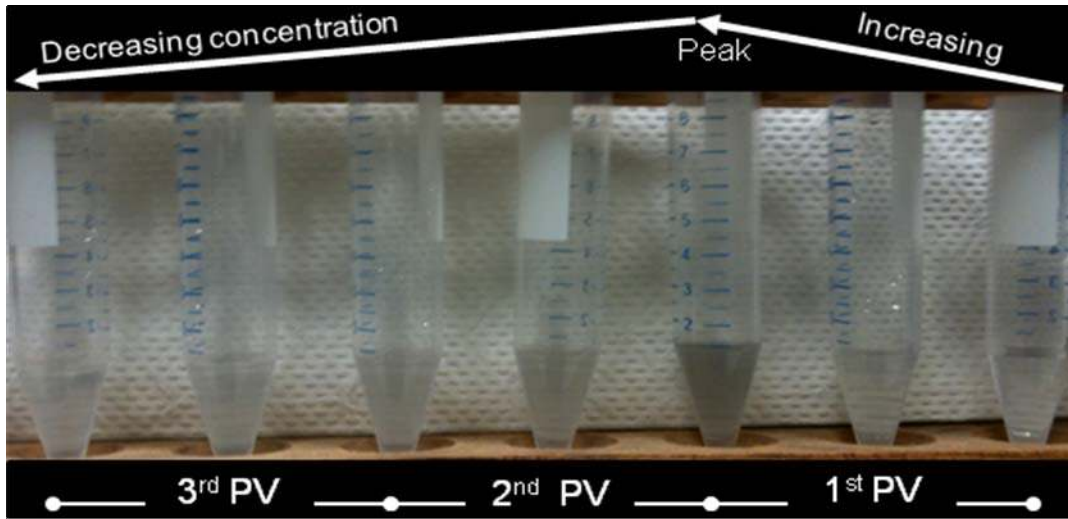
Figure 17: Visual characterization of effluent samples for their tin-bismuth nanoparticles content based on color.
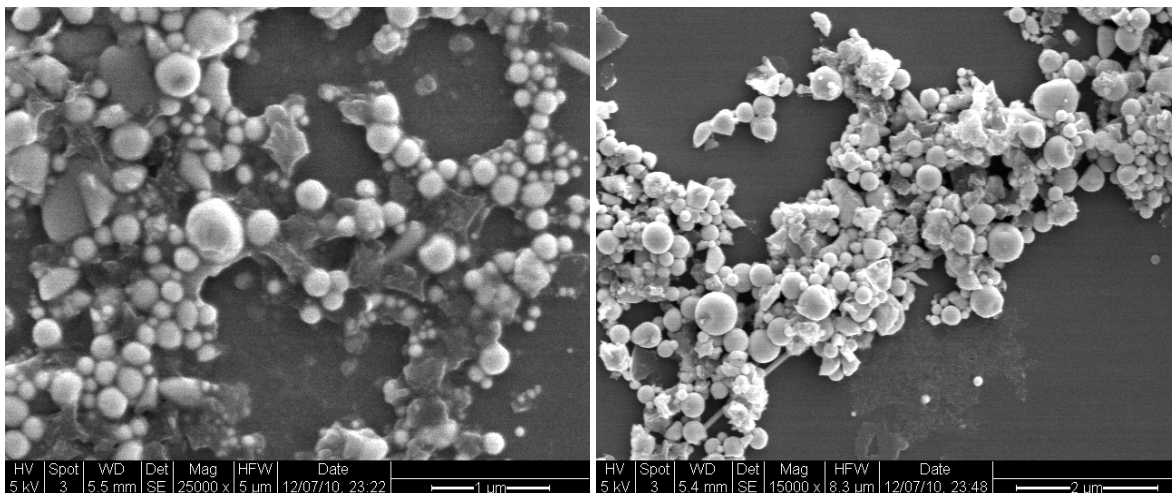

Figure 18: SEM images of the effluent collected during the injection of tin-bismuth nanoparticles into the slim tube packed with glass beads.

SILICA NANOPARTICLES WITH COVALENTLY-ATTACHED FLUORESCENT DYE

As silica particles have been proved to have transported through sandstone core successfully, we further changed their surface properties to explore their temperature response. According to the report by Wu et al. (2008), when free fluorescent dye molecule was attached to silica nanoparticles' surface, through energy transfer, the fluorescent properties of these molecules were changed. Therefore, when the covalent bond between fluorescent dye molecule and surface modified silica nanoparticle is broken under high temperature; the difference of fluorescent behavior before and after heating experiment would be detected.

Synthesis of fluorescent dye-attached silica nanoparticles

First, silica nanoparticles (Nanogiant, LLC) were prepared by surface modification. In a typical reaction, 0.5ml of 3-Aminopropyltriethoxysilane (APTS) was added to 100mg silica nanoparticle suspended in 25 ml of toluene under nitrogen and heating to ~95 °C for 4 hours. The resulting particles were washed by centrifugation in ethanol and acetone (10min at 4,400 rpm). Then the particles were dried at ~95°C overnight.

After that, we attached dye molecules (Oregon 488, Invitrogen) to the surface of the modified silica nanoparticles. A suspension of 1.0 mg of the amino-modified Silica nanoparticles in a mixture of 1ml of ethanol and 15 µl of a 10mmol/L phosphate buffer (pH 7.3) was reacted with 12.7 µl of dye molecule

solution (1mg/ml water solution) in dark for 3 hours at room temperature. The resulting particles were washed by centrifugation (10min at 4,400 rpm) in ethanol and acetone.
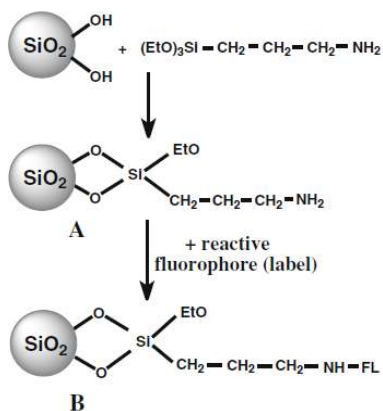

Figure 19: Schematic representation of silica nanoparticle surface modification and dye attachment by Saleh, et al. (2010).

We also performed surface modification and dye attachment reaction on a monolayer of silica nanoparticles on quartz substrate using the same experiment parameters.

Characterization of silica nanoparticles

We used Fluorescent Microscopy, SEM and Fluorescent Spectrum to characterize the dye-attached silica nanoparticles.

Fluorescent microscopy characterization as shown in Figure 20 was done using the substrate base dye-attached silica nanoparticle sample. We can see clearly that the dye molecules were attached successfully to the surface of silica nanoparticles. The whole substrate was fluorescent although not uniformly (some spots were brighter with more fluorescent molecules attached).
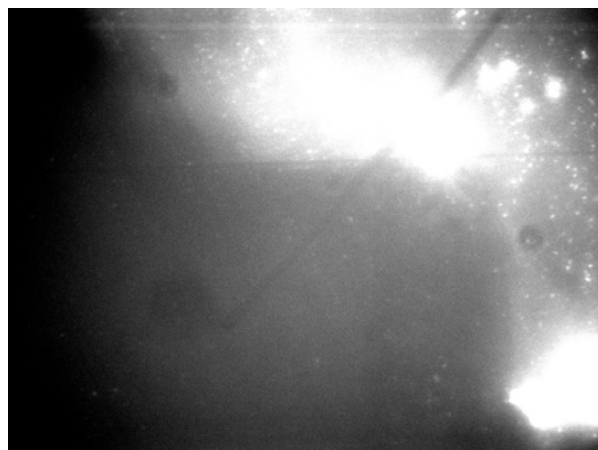

Figure 20: Fluorescent microscopy image of dye-attached silica nanoparticles on quartz substrate.

SEM was also used for characterization.

We also measured the fluorescence spectra of free dye molecule solution, silica nanoparticle suspension, dye-attached silica nanoparticles both on substrate and in solution.

We used 400nm as the excitation wave length. We could see from the fluorescence spectrum of Oregon 488 solution that its emission peak is at ~530nm, shown in Figure 21.

As control, we measured the fluorescence spectrum of silica nanoparticles in water without dye attachment. We also measured the fluorescence spectra of dye-attached silica nanoparticles in water and on substrate. We used 400nm as excitation wavelength, shown in Figure 22. The results showed that, without dye attachment, there was no fluorescence response of the silica nanoparticles and after dye attachment, two peaks at ~425nm and ~530nm were observed in the spectrum.
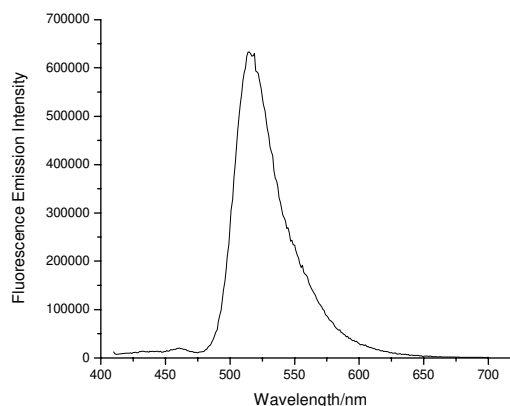

Figure 21: Fluorescence spectrum of Oregon 488 dye molecule solution (excitation wavelength 400nm).
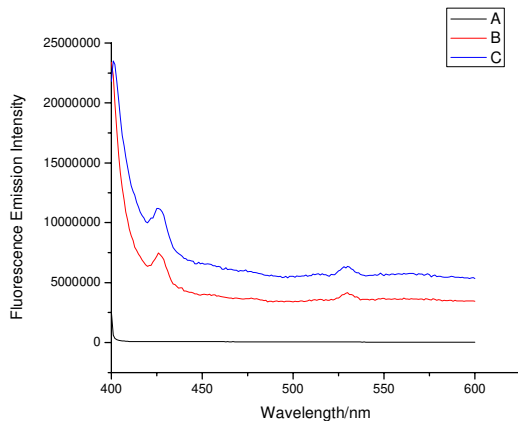
Figure 22: Fluorescence spectrum (excitation wavelength 400nm): (A) Silica nanoparticle without dye attachment as control; (B) Dye-attached silica nanoparticles in water; (C) Dye-attached silica nanoparticles on quartz substrate.
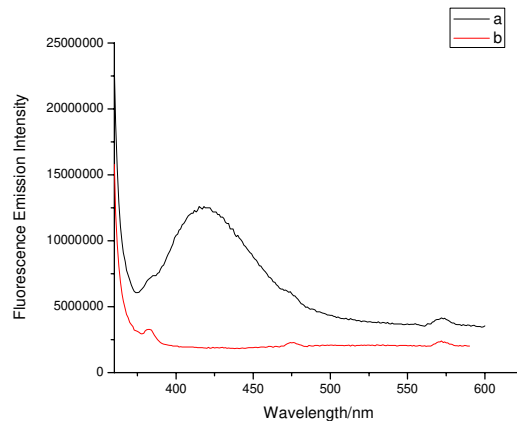

Figure 23: Fluorescence spectrum (excitation wavelength 360nm): (a) Dye-attached silica nanoparticle after heating experiment at 200°C for 15min; (b) Dye-attached silica nanoparticle without heating experiment.

Heating experiment of dye-attached silica nanoparticle

A heating experiment was conducted using the sample of dye-attached silica nanoparticles on quartz substrate. We heated the substrate on a hot plate at 200°C for 15min. Then we soaked the substrate in ethanol and acetone respectively and washed the substrate both with ethanol and acetone. The substrate was dried in air. We used Fluorescence Spectrum to characterize this sample.

Fluorescence spectrum was measured after heating test, shown in Figure 23. We used an excitation wavelength of ~360nm. We can observe a wide peak at ~425nm of the heated sample which was obviously different from the sample before heating. Besides that, we observed at ~380nm and ~475nm there were two shoulder peaks and at ~575nm there was a small peak in both spectra.

Hence, a clearly identifiable property change (fluorescence) is available as a temperature indicator using this kind of nanoparticle.

PROMISING SMART NANOTRACER CANDIDATES

In addition to experimental work, a review of material science literature regarding temperature sensors revealed some potential candidates for geothermal applications. Here we discuss two of the most promising candidates: dye-releasing silica nanoparticles with melting shells and time-temperature indicators.

Hollow silica nanoparticles with encapsulated dye and impermeable melting shells

As it is common practice to use fluorescent dyes as tracers in geothermal reservoirs, a dye-release temperature-sensing scheme would be a convenient means of measuring temperature. Additionally, if a thermally stable dye with sufficiently low detection limits were employed, this sensing scheme would eliminate the need for nanoparticle collection at the production well, which is a significant technical challenge.

Botterhuis et al. (2006) have synthesized hollow silica spheres with encapsulated dye and demonstrated controlled-release behavior in aqueous media. The dye release was found to exhibit two types of behavior: rapid release of dye immobilized in the meso- and macropores via diffusion, and slow, steady release of dye incorporated into the silica walls after the walls dissolved around it.

If these hollow silica nanoparticles were coated with a material impermeable to dye diffusion and with an appropriate melting point, temperature-sensitive dye release could be achieved for geothermal

applications, as illustrated in Figure 24. Possible candidates for the coating material include tin-bismuth and polymers with melting points in the temperature range of geothermal interest.
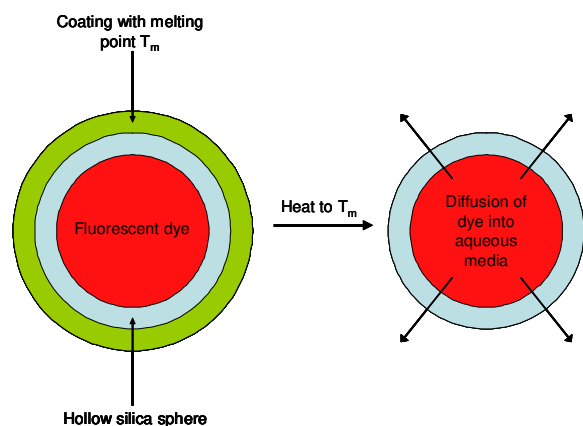

Figure 24: Cartoon of dye-release scheme triggered by the melting of an impermeable shell.

Technical challenges anticipated include development of a suitable coating process, the precision of temperature measurement, and particle mobility in reservoir rock. Before addressing these challenges, we intend to develop a proof of concept using a coating that is sensitive in a lower temperature regime.

Time-temperature indicators

Sing, Weder, and Kunzelman (2009) have developed time-temperature indicators (TTIs) that have been demonstrated to work in high temperature regimes (130°C – 200°C). As most temperature sensors in the literature operate in lower temperature ranges found in biomedical applications, these sensors are perhaps the most promising of those reviewed. These TTIs are films of dye/polymer blends that undergo irreversible fluorescence changes when heated above the glass transition temperature T_g of the polymer, as illustrated in Figure 25.

In the reviewed work, the dyes 4,4'-bis(2-benzoxazolyl)stilbene or cyano-substituted oligo(*p*-phenylene vinylene) were kinetically trapped in thermodynamically unstable dispersed states within ethylene/norbornene copolymers by quenching the blend below T_g during synthesis. Heating the TTIs above T_g caused irreversible phase separation to occur by means of dye aggregation. This aggregation allowed excimers to form and charge-transfer interactions to occur, resulting in permanent changes in fluorescence.
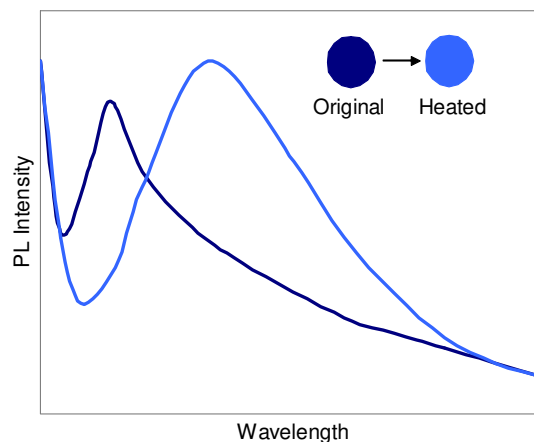

Figure 25: Cartoon of permanent photoluminescence (PL) emission spectral shift that occurs upon heating of TTIs, as shown by Sing, Weder, and Kunzelman (2009).

The kinetics of dye aggregation upon heating exhibited predictable behavior, with the kinetic rate constant following Arrhenius-type temperature dependence. Moreover, the time scale of aggregation can be tuned between seconds and days by changing the dye concentration, choice of dye, or choice of host polymer. Thus, TTIs show potential for providing information about the time of exposure to a given temperature, which could be used to estimate the location of the thermal front within a geothermal reservoir.

We anticipate three main technical challenges regarding the development of TTIs for geothermal applications. The first is the synthesis of nano- or microparticles of the dye-polymer blends with the same capabilities, as the sensors described by Sing, Weder, and Kunzelman (2009) are films, not particles. The second is the precision with which such a sensor can measure reservoir temperature. The third is particle mobility through reservoir rock. We aim to address these challenges and evaluate this candidate according to a full set of criteria in future work.

CONCLUSIONS

We have synthesized two types of temperature-sensitive nanoparticles and demonstrated their sensitivity in the geothermal temperature range. The two types are melting tin-bismuth alloy nanoparticles and silica nanoparticles with dyes incorporated using a temperature-sensitive covalent linkage.

Tin-bismuth alloy nanoparticles were synthesized using a sonochemical method. A heating experiment was performed using these nanoparticles, and particle growth was observed, which was indicative of melting. The flow characteristics of the tin-bismuth nanoparticles were also investigated. Tin-bismuth

nanoparticles of all sizes were transported successfully through the slim-tube. However, when nanoparticles were injected into a Berea sandstone core, only particles with diameters of 200 *nm* and smaller were detected at very low concentrations in the effluent. Nanoparticle plugging and bridging was detected at the core inlet. As measurements of the particle size and surface charge did not indicate any flow constraints, entrapment was attributed either to an affinity of the tin-bismuth to the sandstone rock matrix or an excessively high nanoparticle concentration at the inlet, or both.

Moreover, dye-attached silica nanoparticles were synthesized through surface modification and fluorescent reaction. We demonstrated the successful synthesis by SEM and fluorescence spectrum characterization. A heating experiment was also conducted using a sample of silica nanoparticles on substrate. The results showed that the fluorescence spectra of dye-attached silica nanoparticles in water and on quartz substrate are the same. After heating, the fluorescence spectrum showed an obvious difference at a wavelength of 425nm. Although the mechanism of this phenomenon is not fully understood yet, we did discover the excellent potential of dye-attached silica nanoparticles as temperature sensors for geothermal applications.

Although not tested physically yet, we propose two additional smart tracers targeted for future development: dye-releasing silica nanoparticles with melting shells and time-temperature indicators (TTIs). The former offers the convenience of fluorescence spectroscopy in lieu of particle collection, and the latter has already been proven to work in high temperature regimes (although with films rather than particles).

REFERENCES

Alaskar, M., Ames, M., Horne, R.N., Li, K., Connor, S. and Cui, Y.: "In-situ Multifuction Nanosensors for Fractured Reservoir Characterization," GRC Annual Meeting, Sacramento, USA, vol. 34 (2010).

Botterhuis, N., Sun, Q., Magusin, P., Santen, R. and Sommerdijk, N.: "Hollow Silica Spheres with an Ordered Pore Structure and Their Application in Controlled Release Studies," *Chem. Eur. J.* 2006, **12**, 1448-56.

Chen, H., Li, Z., Wu, Z. and Zhang, Z.: "A novel route to prepare and characterize Sn-Bi nanoparticles," *Journal of Alloys and Compounds.* 2005, **394**, 282-285.

Digital image. Phase Diagrams & Computational Thermodynamics. The National Institute of Standards and Technology. Web. 7 July 2010. <http://www.metallurgy.nist.gov/phase/solder/bisn.html>.

Kanj, M., Funk, J., and Al-Yousif, Z.: "Nanofluid Coreflood Experiments in the Arab-D," SPE paper 126161, presented at the 2009 SPE Saudi Arabia Technical Symposium and Exhibition held in Saudi Arabia, Alkhobar, May 09-11.

Reich, M., Utsunomiya, S., Kesler, S.E., Wang, L., Ewing, R.C., and Becker, U.: "Thermal behavior of metal nanoparticles in geologic materials," Geol. Soc. Am. **34**(2006).

Saleh, S.M., Muller, R., Mader, H.S., Duerkop, A., Wolfbeis, O.S.: "Novel multicolor fluorescently labeled silica nanoparticles for interface fluorescence resonance energy transfer to and from labeled avidin," *Anal Bioanal Chem* (2010) 398:1615-1623.

Sing, C., Kunzelman, J., and Weder, C.: "Time-temperature indicators for high temperature applications," *J. Mater. Chem.* **19** (2009).

Wu, E.C., Park, J.H., Park, J., Segal, E., Cunin, F., and Sailor, M.J.: Oxidation-triggered release of fluorescnct molecules or drugs form mesoporous Si Microparticles," *ACS Nano* (2008), Vol.2 No.11:2401-2409.